

Effect of Rashba spin-orbit and Rabi couplings on the excitation spectrum of binary Bose-Einstein condensates

Rajamanickam Ravisankar^{1,2}, Henrique Fabrelli³, Arnaldo Gammal³,
Paulsamy Muruganandam² and Pankaj Kumar Mishra¹

¹*Department of Physics, Indian Institute of Technology, Guwahati 781039, Assam, India*

²*Department of Physics, Bharathidasan University, Tiruchirappalli 620024, Tamilnadu, India*

³*Instituto de Física, Universidade de São Paulo, 05508-090 São Paulo, Brazil*



(Received 8 July 2021; accepted 28 October 2021; published 17 November 2021)

We present the collective excitation spectrum analysis of binary Bose-Einstein condensates (BECs) with spin-orbit (SO) and Rabi couplings in a quasi-two-dimensional system. In particular, we investigate the role of SO and Rabi coupling strengths in determining the dynamical stability of the coupled BECs using Bogoliubov–de Gennes (BdG) theory. Using the eigenenergy of the BdG spectrum, we confirm the existence of phonon, roton, and maxon modes with weak repulsive intra- and interspecies contact interactions. The depth of the minimum corresponding to the roton mode strongly depends on the coupling strength. We find that the increase of the SO coupling leads to instability, while the increase in the Rabi coupling stabilizes the system. Also, the eigenvectors of the BdG spectrum indicate the presence of a densitylike mode in the stable regime and spinlike modes in the unstable regimes. A phase diagram demonstrating the stability regime in the plane of SO and Rabi coupling strengths is obtained. Finally, we complement the observation of the excitation spectrum with the direct numerical simulation results of coupled Gross-Pitaevskii equations.

DOI: [10.1103/PhysRevA.104.053315](https://doi.org/10.1103/PhysRevA.104.053315)

I. INTRODUCTION

The experimental realization of Bose-Einstein condensates (BECs) in dilute atomic gases has triggered immense interest in the physics of ultracold matter [1–3]. Since then, BECs has become an excellent system for manipulating many of the macroscopic phenomena through the controlled environment in the quantum regime. The last few decades have seen an upsurge in the research of BECs, in particular to understand the fundamental and dynamical aspects of solitons, its behavior under the optical lattice and disordered potentials trap, superfluid-Mott insulator phase transition, presence of localization, dipolar and spin-orbit (SO) coupled BECs [4–14], etc. In this paper, we investigate the effect of the Rabi and Rashba spin-orbit (SO) coupling on the dynamical stability of the binary BECs system.

In BECs, the internal atomic states can be manipulated to produce quite novel systems such as binary and multicomponent condensates. These binary or multicomponent BECs consist of different isotopes or hyperfine states of the same or different atomic species, which are coherently coupled by the external fields [15–17]. This facilitates the testing ground of a plethora of macroscopic quantum many-body phenomena such as quantum turbulence [18], quantum phase transitions [19], quantized vortices, matter wave solitons [20], vortex-antivortex [21], etc. BECs of bosons in two different hyperfine states, designated as spin-1/2 bosons, have opened up a new way for synthetic SO coupling, a key ingredient for many important condensed matter phenomena. In this connection, the realization of SO coupled Bose and Fermi gases at ultralow temperature has paved the way for many important

physical phenomena of current interest such as measurement of the spin Hall effect [14,22], topological insulators [23], topological superfluids [24], atomtronics (or spintronics) [25], and quantum computing [26].

Numerical simulations have played an important role in unraveling different interesting phases in coupled BECs. The stability and dynamics of matter-wave bright and dark solitons in one-dimensional SO coupled BECs have been investigated quite extensively using coupled Gross-Pitaevskii equations (GPEs) [27–30]. In two dimensions, Rashba SO coupled BECs with weak harmonic trap exhibit plane- and stripe-wave phases, while, under a strong harmonic trap, it displays the presence of vortex pairs, honeycomb-lattice and half-quantum vortices, upon varying the Rabi coupling strength [31]. The SO coupled BECs confined in the optical lattice reveal different ground-state structures as the form of a vortex-antivortex pair [32]. Using the numerical and variational analysis, Cheng *et al.* demonstrated that SO coupled BECs trapped under bichromatic optical lattices show Anderson localization [33]. It was found that the Rabi coupling stabilizes the superfluid phase in coupled BECs in optical lattices [34]. A variety of collective modes, namely, Nambu-Goldstone, slosh, and bifurcation modes, was studied in the trapped two-component quasi-two-dimensional (quasi-2D) BECs [35,36].

The stability of different ground-state phases of SO coupled BECs could be well understood by analyzing the spectrum of elementary excitation. For instance, the Bogoliubov–de Gennes (BdG) spectrum, much related to macroscopic quantum phenomena, such as superfluidity and superconductivity, provides the fundamental information about the condensate dynamics. The excitation spectrum of

BECs with Rashba-Dresselhaus SO coupling was found to exhibit roton-maxon structures [37–42]. Using the Green’s function technique, various interesting features, such as multicriticality, metastability, and the roton, were found to exist in three-dimensional Rashba SO coupled BECs [43]. The metastability could be understood as a result of the absence of imaginary frequencies in the BdG spectrum [44]. Ozawa *et al.* numerically investigated the dynamical and energetic instabilities in quasi-1D SO and Raman coupled BECs [45]. Spin-dipole and breathing modes of the collective excitation spectrum give a clear picture of phase boundaries, which was also confirmed by the quenching dynamics numerically [46]. The effect of SO, Rabi couplings, and nonlinear interactions provides collective oscillations, which have a transition from the harmonicity to the anharmonicity [47]. In a recent work, Geier *et al.* found the signature of Goldstone modes in harmonically trapped SO coupled BECs [48].

The application of the BdG spectrum was studied in the context of exploring the superfluid phase in SO coupled BECs [49]. Further, Yu *et al.* used this idea in obtaining the ground-state phase diagram, particularly excitations of zero momentum phases in quasi-2D SO coupled BECs [50]. Another interesting aspect of the binary SO coupled BECs is the appearance of droplet formation, also popularly known as quantum droplet in the isotropic mixture of binary BECs [51]. Petrov analytically demonstrated that in a quantum droplet, the mean-field collapsing interaction is stabilized by the quantum fluctuations contributed through the beyond-mean-field term [52]. Recently, Sahu and Majumdar numerically reported the effect of SO couplings on the stability of the BdG spectrum of the quantum droplet in quasi-2D and found the presence of different excitation modes, such as phonon, roton, and double roton modes, with different SO couplings as the interaction strengths are varied [53].

The excitation spectrum holds a vital clue about the presence of superfluidity and supersolid behavior. In particular, the appearance of roton softening in the excitation spectrum can be attributed to the supersolid nature. In a system of two-dimensional dipolar bosons with two- and three-body interactions, it has been demonstrated that the roton-maxon modes yield a dilute supersolidlike state [54]. The presence of ground states such as supersolid and stripe supersolid phases has also been realized in the SO coupled BECs trapped under optical superlattices [55]. We primarily consider the homogeneous case to analyze the collective excitations in two-dimensional SO coupled BECs. It was also shown that the roton-maxon mode in the excitation spectrum reveals the appearance of the supersolid nature due to the superposition of spin components at the two minima of the excitation spectrum [40].

It may be noted that most of the studies of the collective excitations are mainly focused on quasi-1D spin-orbit coupled BECs [37–42] and limited explorations are available on the stability of the superfluid phases in two dimensions [56]. For obvious reasons, it would be more appropriate to study collective excitations in higher spatial dimensions. In this paper, we present a detailed study of the stability analysis of SO coupled BECs in two dimensions from the excitation spectrum of BdG equations. In particular, we carry out a systematic analysis of collective excitations of SO coupled BECs in

quasi-two dimensions using the dispersion relations obtained by the application of Bogoliubov theory to the coupled Gross-Pitaevskii (GP) equations. These dispersion relations are then used for the stability analysis of plane waves, phonon-maxon-roton excitations, and the interplay between SO and Rabi couplings. Note that the appearance of the roton mode may be attributed to the precursor of the stripe phase with periodic fringes, an essential ingredient of supersolids [37,42], while instability signifies the existence of matter-wave solitons.

The paper is organized as follows. In Sec. II, we introduce a mean-field theoretical model used to study the SO coupled BECs in quasi-two dimensions. In Sec. III, we analytically derive the single-particle dispersion relation. Following this, using the Bogoliubov–de Gennes method, we investigate the collective excitation of Rashba SO coupled BECs analytically and numerically by computing the eigenspectrum and eigenvectors in Sec. IV. The numerical simulation of the stability analysis of the ground state obtained by solving the coupled GP equations of quasi-two-dimensional Rashba SO coupled BECs is presented in Sec. V. Finally, in Sec. VI, we conclude our observation of the SO coupled BECs.

II. MEAN-FIELD MODEL OF COUPLED BECS

We consider pseudospin-1/2 Bose-Einstein condensates with Rashba spin-orbit and Rabi coupling, which Hamiltonian is given by [31]

$$\mathcal{H} = \mathcal{H}_0 + \mathcal{H}_I, \quad (1)$$

with

$$\mathcal{H}_0 = \int \Psi^\dagger \left[\frac{\mathbf{p}^2}{2m} + V + k'_L \mathbf{p} \cdot \boldsymbol{\sigma} + \Omega' \sigma_x \hbar \right] \Psi d\mathbf{r}, \quad (2)$$

$$\mathcal{H}_I = \int \left[\frac{g_{\uparrow\uparrow}}{2} |\Psi_\uparrow|^2 + \frac{g_{\downarrow\downarrow}}{2} |\Psi_\downarrow|^2 + g_{\uparrow\downarrow} |\Psi_\uparrow| |\Psi_\downarrow| \right] d\mathbf{r}. \quad (3)$$

Here, $\Psi = (\Psi_\uparrow \ \Psi_\downarrow)^T$ is the two-component spinor normalized wave functions that satisfy the condition $\int (|\Psi_\uparrow|^2 + |\Psi_\downarrow|^2) d\mathbf{r} = N$, with N being the total number of particles, m the atomic mass, and $\mathbf{p} = -i\hbar\nabla$ the momentum operator; $\boldsymbol{\sigma} = (\sigma_x, \sigma_y)$ are the 2×2 Pauli matrices, and $g_{\uparrow\uparrow}$ and $g_{\downarrow\downarrow} = 4\pi a\hbar^2/m$, ($a = a_{\uparrow\uparrow} = a_{\downarrow\downarrow}$), $g_{\uparrow\downarrow} = 4\pi a_{\uparrow\downarrow}\hbar^2/m$ are the intra- and interspecies contact interaction strengths, with a and $a_{\uparrow\downarrow}$ being the intra- and interspecies s -wave scattering lengths, respectively. We consider the condensates confined in the harmonic trap potential with form $V = m[\lambda^2 x^2 + \kappa^2 y^2 + \eta^2 z^2]/2$, where the trap aspect ratios are $\lambda = \omega_x/\omega_\perp$, $\kappa = \omega_y/\omega_\perp$, and $\eta = \omega_z/\omega_\perp \gg 1$.

In order to study the ground-state and dynamical properties of Rashba SO coupled BECs with strong axial traps, we consider the two-dimensional coupled GP equations in dimensionless form as

$$i \frac{\partial \psi_\uparrow}{\partial t} = \left[-\frac{1}{2} \nabla^2 + V_{2D}(x, y) + \alpha |\psi_\uparrow|^2 + \beta |\psi_\downarrow|^2 \right] \psi_\uparrow - \Lambda_+^{\text{SO}} \psi_\downarrow, \quad (4a)$$

$$i \frac{\partial \psi_\downarrow}{\partial t} = \left[-\frac{1}{2} \nabla^2 + V_{2D}(x, y) + \beta |\psi_\uparrow|^2 + \alpha |\psi_\downarrow|^2 \right] \psi_\downarrow - \Lambda_-^{\text{SO}} \psi_\uparrow, \quad (4b)$$

where $\nabla^2 = \partial_x^2 + \partial_y^2$, $V_{2D}(x, y) = (\lambda^2 x^2 + \kappa^2 y^2)/2$ is the harmonic trap potential and $\Lambda_{\pm}^{SO} = [k_L(i\partial_x \pm \partial_y) + |\Omega|]$. In the above Eqs. (4), length is measured in units of harmonic oscillator length $a_0 = \sqrt{\hbar/(m\omega_{\perp})}$, time in units of ω_{\perp}^{-1} , and energy in units of $\hbar\omega_{\perp}$. The parameters $\alpha = \sqrt{8\pi\eta}Na/a_0$ and $\beta = \sqrt{8\pi\eta}Na_{\uparrow\downarrow}/a_0$ represent intra- and interspecies contact interaction strengths, respectively. The Rashba SO coupling and the Rabi coupling parameters have been rescaled as $k_L = k'_L/a_0\omega_{\perp}$ and $\Omega = \Omega'/\omega_{\perp}$, respectively, while the wave function is rescaled as $\psi_{\uparrow,\downarrow} = \Psi_{\uparrow,\downarrow}a_0^{3/2}/\sqrt{N}$. We consider the Rabi coupling as $\Omega = |\Omega|e^{i\theta}$ that minimizes the energy when $\Omega = -|\Omega|$ for $\theta = \pi$ [57]. The wave functions are subjected to the following normalization condition:

$$\int_{-\infty}^{\infty} \int_{-\infty}^{\infty} (|\psi_{\uparrow}|^2 + |\psi_{\downarrow}|^2) dx dy = 1. \quad (5)$$

The stationary state solution of the wave function is given by

$$\psi_j(x, y) = (\psi_{jR} + i\psi_{jI})e^{-i\mu_j t}, \quad (6)$$

where $j \in \{\uparrow, \downarrow\}$, ψ_{jR} and ψ_{jI} are the real and imaginary parts of the stationary wave function, respectively, and $\mu_{\uparrow,\downarrow}$ are the chemical potentials of the spin-up and -down components, respectively. Now, using Eqs. (4a), (4b), and (6), the ground-state energy of the Rashba SO coupled BECs can be obtained as

$$E_{\text{num}} = \sum_{j=\uparrow,\downarrow} \frac{\iint (E_j^{2C} + E_j^{SO}) dx dy}{\iint \psi_{jR}^2 dx dy}. \quad (7)$$

The detailed form of the E_j^{2C} and E_j^{SO} is given in Appendix A.

Following the experiment with ^{87}Rb condensates confined in the harmonic trap with frequencies $(\omega_{\perp}, \omega_z) = 2\pi \times (50, 140)$ Hz in the radial and axial directions, respectively [13], we consider $N \sim 10^5$ atoms. The characteristic length scale can be obtained as $a_0 \approx 3 \mu\text{m}$ and the scattering length is $a = a_{\uparrow\downarrow} = 0.35a_B$, where a_B is the Bohr radius and can be tuned by using the Feshbach resonance and with a suitable magnetic field [9], which provides the dimensionless interaction strength $\alpha = \beta \approx 1$. We consider the Rabi coupling parameter in the range of $\Omega' = \{0 - 2\}\omega_{\perp}$, which usually couples the spin states by tuning the frequency of Raman lasers and the spin-orbit coupling strength. The Rashba SO coupling range is $k'_L = \{0 - 2\}a_0\omega_{\perp}$, which can be varied with the Raman laser wavelength and geometry.

In the following, at first we provide a detailed analysis of the single-particle spectrum both in the k_x and k_y momentum directions. Next, we present analytical and numerical studies of the collective excitation spectrum to investigate the stability of the ground states obtained from the coupled GP Eqs. (4a) and (4b) as the small fluctuation is added in the ground state. This is followed by a detailed numerical analysis of the dynamics of the ground states.

III. SINGLE-PARTICLE SPECTRUM

In this section, first we present the calculation of two-component coupled GP equations with Rashba SO coupling for noninteracting BECs without any trapping potential, which gives the ‘‘single-particle spectrum.’’ Following this,

we include the intra- and interspecies nonlinear contact interactions with small perturbation, which gives rise to the ‘‘excitation spectrum’’ of the coupled system. This also includes the interesting features that appear due to the interplay of Rashba SO (k_L) and Rabi couplings (Ω).

Let us consider Eqs. (4a) and (4b) in the absence of trap and contact interaction strengths (i.e., $V = \alpha = \beta = 0$) and use the plane-wave solution $\psi_{\uparrow,\downarrow} = \phi_{\uparrow,\downarrow}e^{i(k_x x + k_y y - \nu t)}$ in the computational basis. We get

$$\nu = \begin{pmatrix} \frac{1}{2}(k_x^2 + k_y^2) & k_L(k_x - ik_y) - |\Omega| \\ k_L(k_x + ik_y) - |\Omega| & \frac{1}{2}(k_x^2 + k_y^2) \end{pmatrix}, \quad (8)$$

which gives the single-particle energy spectrum ν from Eq. (8) as

$$\nu(\mathbf{k})_{\pm} = \frac{1}{2}(k_x^2 + k_y^2) \pm \sqrt{(k_L k_x - |\Omega|)^2 + k_L^2 k_y^2}. \quad (9)$$

The single-particle spectrum have two branches. First is the positive branch (ν_+), which always has the single minimum, and second is the negative branch (ν_-), which makes a transition from the single minimum to the double minima as the SO coupling strength (k_L) is increased for a fixed Rabi coupling. In what follows, we focus our study on analyzing the negative branch as it exhibits a transition between the single minimum to the double minima. We analyze the spectrum with respect to the k_x and k_y momentum directions, which will be useful to clearly analyze the phase transition.

In k_x direction. For zero Rabi and SO couplings ($\Omega = k_L = 0$), the spectrum is a nondegenerate parabolic single-particle dispersion spectrum [Fig. 1(a)], which can also be seen from Eq. (9). However, the spectrum exhibits double minima characteristics for finite values of the SO coupling strength (k_L). The minima are located at the position $k_x = \pm k_L$ [Fig. 1(c)]. The value of the energy minima increases with the SO coupling strength as $\pm k_L^2/2$. For nonzero Rabi coupling ($\Omega \neq 0$) and $k_L = 0$, the spectrum exhibits a single minimum and develops an energy gap between ν_{\pm} which is equal to 2Ω [Fig. 1(e)]. However, for nonzero k_L , the spectrum develops asymmetric double minima as shown in Fig. 1(g). As the Rabi coupling is increased, the system attains the minimized energy state. For example, with $k_L = 0.7$ and $\Omega = 0.5$, the spectrum has a global minimum with $\nu_- = -0.745$ [see Fig. 1(g)]. Further increase in Rabi coupling from $\Omega = 0.5$ to 0.7 results in lowering the energy state to $\nu_- = -0.945$ [Fig. 1(i)]. As Ω is increased further, the spectrum develops a global minimum and the corresponding energy varies as $k_L^2/2 + \Omega$.

For the fixed Rabi coupling $\Omega = 0.5$, as we change the SO coupling strength from $k_L = 0.7$ to $k_L = 1.0$, we find that the energies change from single minimum ($\nu_- = -0.745$) to double minima ($\nu_- = \{-1.0, 0\}$). It suggests that in general, the atoms will get condensate in the lowest-energy state, i.e., global minimum [see Fig. 1(i)]. While increasing k_L , we found two minima with opposite wave vectors which will form stripelike patterns [see Fig. 1(k)].

In k_y direction. The spectrum exhibits two minima in the absence of Rabi coupling with a finite k_L [see Fig. 1(d)]. The spectrum is typically known as the *Rashba ring* in 2D momentum space [31,56]. As the Rabi coupling is increased for fixed k_L , a transition from the double minima state to the single minimum state is observed at critical $\Omega(\approx k_L^2)$, while

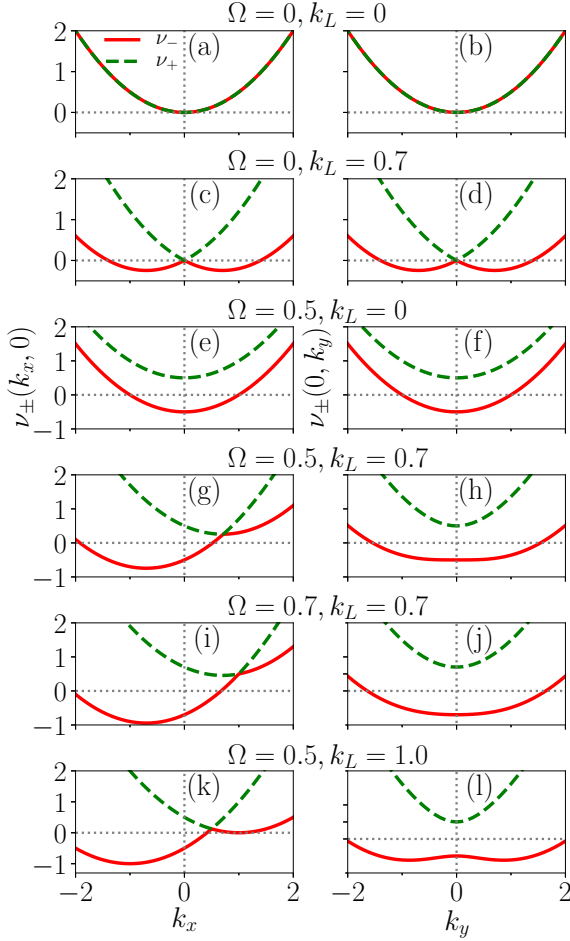


FIG. 1. Single-particle energy spectrum in the $\{k_x, k_y\}$ momentum space for different sets of coupling parameters indicated in the figure. Left column indicates $\nu_{\pm}(k_x, 0)$ with $k_y = 0$ and right column shows $\nu_{\pm}(0, k_y)$ for fixed $k_x = 0$. Solid red line shows $\nu_{-}(k_x, k_y)$ and green dashed line is for $\nu_{+}(k_x, k_y)$. Note that all the quantities reported in this and subsequent figures are in the nondimensional unit. The nondimensionalized scheme is discussed in Sec. II.

the symmetry of the system remains unchanged. We find that the energy gap between these two energy spectra is 2Ω as shown in Figs. 1(h) and 1(j). The energy of the system gets lowered as Rabi coupling is increased. For an example, as the coupling parameter is changed from $\Omega = 0.5$ to $\Omega = 0.7$ for a fixed $k_L = 0.7$, the spectrum energies change from $\nu_{-} = -0.5$ to $\nu_{-} = -0.7$ [see Figs. 1(h) and 1(j)]. The energy strongly depends on the Rabi coupling strengths for the cases $\Omega > k_L^2$. However, for $\Omega < k_L^2$, the energy depends on SO coupling strengths.

As we perform the energy comparison between the k_x and k_y directions, we find that in the presence of the Rabi coupling, the energy has the lowest value in the k_x direction, indicating the breaking of the rotational symmetry of the single-particle energy spectrum. This feature suggests that the plane-wave spectrum will get sustained with finite momentum for $\Omega > k_L^2$. However, for $\Omega < k_L^2$, the stripe wave will exist. We do not observe any zero-momentum (ZM) phase for $k_L \neq 0$, which was realized in the one-dimensional SO coupled BEC [58,59]

and in two-dimensional BECs [31,60] with nonlinear contact interactions.

In the following section, we investigate the effect of couplings on the excitation spectrum of the SO coupled BECs.

IV. ANALYSIS OF THE EXCITATION SPECTRUM OF RASHBA SO COUPLED BECS

In this section, we present our analytical and numerical investigation of the excitation spectrum of the coupled BECs with SO and Rabi couplings. In 1941, Landau initiated the concept of elementary excitation to explain the superfluid behavior in ^4He . The mathematical derivation of the excitation spectrum for the Bose gases was given by Bogoliubov in 1947 [61]. The collective excitation spectrum of BECs gives the basic information about the dynamics of the quantum systems such as superfluid helium [62], superconductors [63], phononlike excitation observed in ^{87}Rb atom in an optical trap [64], and magnetic trap [65]. Here our aim is to investigate the excitation spectrum analytically, which in the latter part of the paper will be complemented with the numerical simulation. At first, we analytically transform the pure ground-state wave function $(\psi_{\uparrow, \downarrow})$ by adding a small perturbation $(\delta\psi_{\uparrow, \downarrow})$. After direct algebraic manipulations, the system appears to have different excitation branches, namely, two positive and two negative branches. We analyze the characteristic of those energy branches by varying the SO and Rabi coupling parameters and further investigate the stability of the different modes.

A. Analytical and numerical description of excitation spectrum

In order to understand the stability of our system, we calculate the excitation spectrum of the plane-wave solutions using the Bogoliubov theory. Let us assume that the total density of the system is $n = n_{\uparrow} + n_{\downarrow}$ and the chemical potential is μ . Therefore, the stationary state evolution can be written as [57,66]

$$\Psi_j = e^{-i\mu t} [\psi_j + \delta\psi_j], \quad (10)$$

$$\delta\psi_j = u_j e^{i(k_x x + k_y y - \omega t)} + v_j^* e^{-i(k_x x + k_y y - \omega^* t)}, \quad (11)$$

where $\psi_j = \sqrt{n_j} e^{i\varphi_j}$, $j = (\uparrow, \downarrow)$ is the ground-state wave function, u_j and v_j are the amplitudes, and n_j and φ_j are the density and phase, respectively. The Bogoliubov coefficients u and v could be obtained by substituting Eq. (10) in Eqs. (4a) and (4b). Therefore, we have

$$\omega(u_{\uparrow} \quad v_{\uparrow} \quad u_{\downarrow} \quad v_{\downarrow})^T = \mathcal{L}(u_{\uparrow} \quad v_{\uparrow} \quad u_{\downarrow} \quad v_{\downarrow})^T, \quad (12)$$

where the superscript T denotes the transpose of the matrix and

$$\mathcal{L} = \begin{pmatrix} f(n_{\uparrow}, n_{\downarrow}) & \alpha n_{\uparrow} & L_{13} & \beta \sqrt{n_{\uparrow} n_{\downarrow}} \\ -\alpha n_{\uparrow} & -f(n_{\uparrow}, n_{\downarrow}) & -\beta \sqrt{n_{\uparrow} n_{\downarrow}} & -L_{24} \\ L_{31} & \beta \sqrt{n_{\uparrow} n_{\downarrow}} & g(n_{\downarrow}, n_{\uparrow}) & \alpha n_{\uparrow} \\ -\beta \sqrt{n_{\uparrow} n_{\downarrow}} & -L_{42} & -\alpha n_{\downarrow} & -g(n_{\downarrow}, n_{\uparrow}) \end{pmatrix}, \quad (13)$$

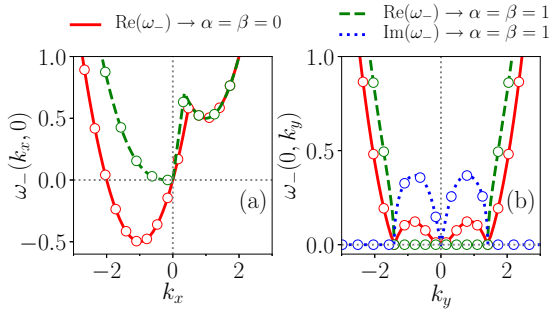


FIG. 2. Collective excited dispersion of $\text{Re}(\omega_-)$ (solid red line) for the noninteracting case and of $\text{Re}(\omega_-)$ (dashed green line) and $\text{Im}(\omega_-)$ (dotted blue line) for the interacting ($\alpha = \beta = 1$) case. The parameters are $\Omega = 0.5$, $k_L = 1$. (a) Variation of negative spectrum along the k_x direction for $k_y = 0$ and (b) variation of negative spectrum along the k_y direction for $k_x = 0$. Solid lines represent the analytical results obtained from BdG Eq. (15) and open circles denote the numerical solution of Eq. (12).

and other coefficients are given in Appendix B. The normalization condition yields

$$\iint (|u_j|^2 - |v_j^*|^2) dx dy = 1. \quad (14)$$

The simplified form of the Bogoliubov–de Gennes equation under the condition $\det \mathcal{L} = 0$ will have the form for the interacting case with $n_\uparrow = n_\downarrow = 1/2$ as

$$\omega^4 + b\omega^2 + c\omega + d = 0. \quad (15)$$

By direct mathematical manipulation of Eq. (15), we obtained four dispersion relations. The complicated expressions of the coefficients (b, c, d) are given in Appendix C.

Following this, we corroborate the analytical results for the excitation spectrum by numerically solving the BdG equations from which we also obtain the eigenvectors as a function of k_x and k_y . First we consider a $[-1000 : 1000][-1000 : 1000]$ grid in real space with step size $h_x = h_y = 0.05$. Then we use the Fourier collocation method where we numerically perform the Fourier transformation of the BdG equations and obtain a truncated reduced BdG matrix, which is subsequently diagonalized using the LAPACK package [67]. In momentum space, we consider $[-50 : 50][-50 : 50]$ modes in the k_x, k_y directions, respectively, with a grid step size of $h_{k_x} = h_{k_y} = 0.0628$.

B. Comparison of excitation spectrum with and without interactions

In the following, we analyze the effect of the couplings on the stability of the negative branch of the energy spectrum. Note that the negative eigenenergy of the excitation spectrum implies that the system is energetically unstable, while the complex eigenenergies indicate the dynamical instability [45]. The BdG excitation spectrum obtained from Eq. (15), without SO coupling ($k_L = 0$), is similar to that obtained in Refs. [57,66]. Apart from this, the dispersion relation has two-dimensional Rashba SO and linear Rabi couplings. Figure 2 shows the system of the collective BdG excitation spectrum. The comparison between the noninteracting (solid

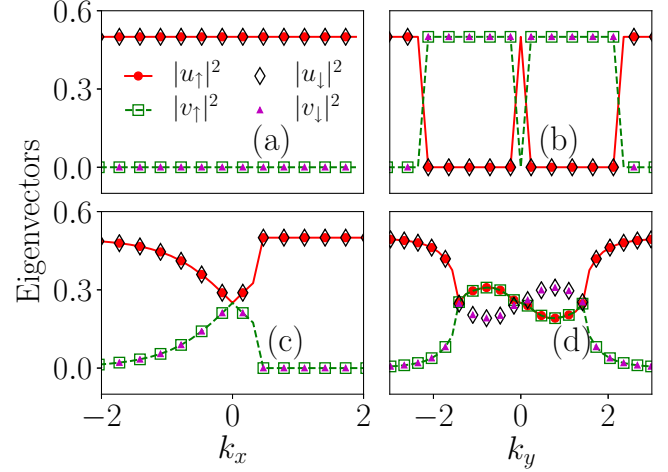


FIG. 3. The eigenvectors obtained by solving Eq. (12): Red dots with solid line for $|u_\uparrow|^2$ component, black open diamond for $|u_\downarrow|^2$, green open square with dashed line for $|v_\uparrow|^2$, and magenta triangle for $|v_\downarrow|^2$. Top row is for the noninteracting case and bottom row is for the interacting case. Left column shows the variation of eigenvectors along the k_x directions and right column those variation along the k_y directions. All the other parameters are the same as in Fig. 2. For the noninteracting case plane wave, the density mode dominates for the entire range of the wave number, while for the interacting case, a transition from the density to spin mode occurs where the negative spectrum becomes complex in the k_y momentum direction.

red lines) and interacting ($\alpha = \beta = 1$) cases (shown with the dashed green and dotted blue lines) indicates that the former case does not have any imaginary part, while the latter case has the imaginary part. This particular feature suggests that the metastability of the plane-wave phase of SO coupled BECs is destroyed in the k_y direction, which makes the system dynamically unstable, indicating the system lacks any superfluid behavior [49].

In Fig. 3, we plot the eigenvectors corresponding to the eigenenergy spectrum as shown in Fig. 2. For the noninteracting case, the in-phase of the eigenvector components for all wave numbers indicates the presence of only densitylike modes (in-phase) in both momentum directions [see Figs. 3(a) and 3(b)]. However, for the interacting case ($\alpha = \beta = 1$), the presence of some complex patterns is observed. There is a transition from the densitylike modes (in-phase) to the spinlike mode (out-of-phase) that takes place in the k_y direction as shown in Figs. 3(c) and 3(d). We find that both eigencomponents of the eigenvectors u and v are in-phase in the k_x direction. For $k_x \approx 0$, the eigenvectors approach each other and have equal values at $k_x = 0$, which indicates the presence of a phonon mode. Beyond this, there is a sudden increase in the value of the eigenvectors. At finite k_x , again there is a change in the curve that corresponds to the maxon point, which is followed by returning to the densitylike mode. In the k_y direction, we found two types of behavior. First, up to the $\text{Re}(\omega_-)$, the u and v are in-phase, while second, the presence of $\text{Im}(\omega_-)$ changes the u and v to out-of-phase, which indicates the presence of a spinlike mode [57].

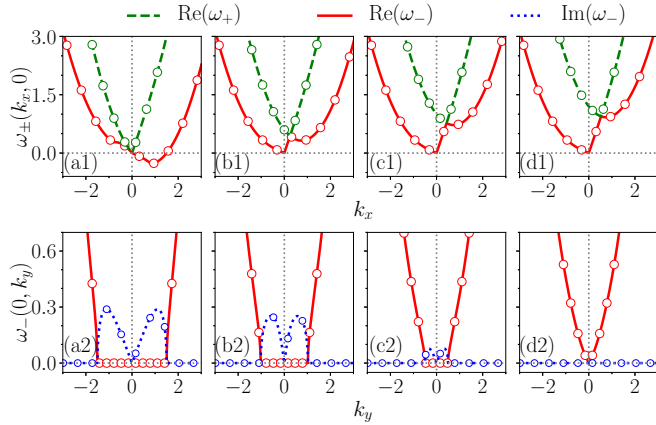


FIG. 4. Excitation spectrum in the k_x (first row) and k_y (second row) momentum directions for different Ω . Ω varies in (a)–(d) = (0, 0.3, 0.5, 0.6) and other fixed parameters are $k_L = 0.75$, $\alpha = \beta = 1$. First row: Solid red line and dashed green line indicate $\omega_-(k_x, 0)$ and $\omega_+(k_x, 0)$, respectively. Second row: Red solid line and dotted blue line depict that $\text{Re}[\omega_-(0, k_y)]$ and $|\text{Im}[\omega_-(0, k_y)]|$, respectively. Solid lines are the analytical results from BdG Eq. (15) and open circles are obtained numerically solving Eq. (12). First row shows roton softening upon increase in Ω , which reflects as a disappearance of the imaginary modes for high Ω .

C. Effect of Rabi coupling on the excitation spectrum

Theoretically, it was noticed that the excitation spectrum of quasi-one-dimensional Raman SO coupled BECs consists of a rotonlike minimum for the case of finite Rabi coupling [37,39], which was also confirmed experimentally in [40–42]. In this section, we present the effect of Rabi coupling on the excitation spectrum in two-dimensional coupled BECs. As Rabi coupling is decreased, we find that beyond the critical value of Ω , a rotonlike minimum starts softening and develops a negative frequency, which indicates the appearance of instability in the system. We fix the SO coupling parameter to $k_L = 0.75$ with $\alpha = \beta = 1$, and vary the Rabi strength Ω . We consider $\Omega = 0, 0.3, 0.5$, and 0.6 . In Fig. 4, we show the dispersion behavior for different Ω by keeping the Rashba coupling (k_L) fixed. We notice the presence of minimum attributed to the phonon, maxon, and roton. At zero Rabi coupling ($\Omega = 0$) strength, the excitation spectrum possesses negative frequency in the k_x direction, indicating that the system is energetically unstable. However, in the k_y direction, the system exhibits dynamical instability due to the presence of the complex excitation frequency. Owing to this feature, at zero Rabi coupling, the system does not exhibit any superfluid behavior [49].

At this point, it is worthwhile to mention that the occurrence of a gapless excitation in some cases has also been observed as a signature of supersolid nature. However, we find that the roton energy minimum is unable to reach the gapless double minima. As an example for $\Omega = 0.14$, the spectrum shows negative excitation energy ($\omega = -0.00125$). However, a small variation in the coupling parameter (i.e., at $\Omega = 0.15$) results in the energy of 0.0875 accompanied by a small gap between the minima. Note that even the roton gapless double minima is present, and the system does not hold the supersolid

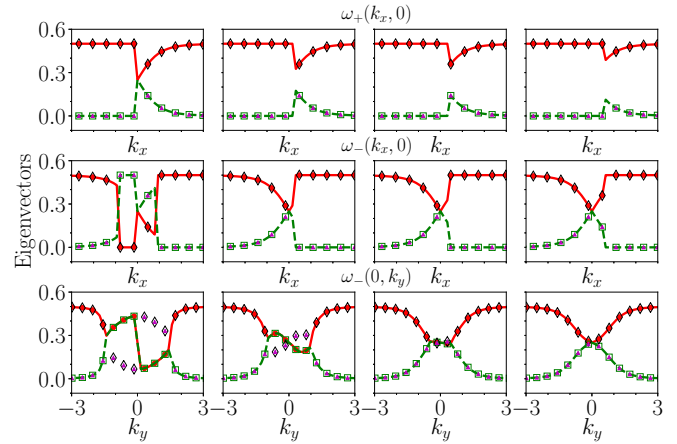


FIG. 5. The eigenvectors corresponding to the eigenspectrum of Fig. 4. Top panel represents the eigenvectors corresponding to $\omega_+(k_x, 0)$ (dashed green line), middle panel for $\omega_-(k_x, 0)$ (solid red line), and bottom panel for $\omega_-(0, k_y)$. The representation of the eigenvector components is the same as in Fig. 3. The maxon mode in the top panel, phonon-maxon mode in the middle panel, and spin to density mode transition in the bottom panel are noticeable.

feature owing to the presence of complex eigenfrequencies which makes the system dynamically unstable.

As the Rabi coupling strength is increased to $\Omega = 0.3$, the eigenfrequency suggests the presence of a minimum related to the phonon-maxon-roton modes in the k_x direction, while in the transverse direction (k_y), it suggests the presence of the complex eigenfrequencies [see Figs. 4(b1) and 4(b2)]. This behavior indicates the dynamically unstable state for this SO coupling strength. For $\Omega = 0.5$, the system remains dynamically unstable; however, a decrease in the roton minimum and amplitude of the imaginary frequency is observed [see Figs. 4(c1) and 4(c2)].

As the Rabi coupling strength is increased beyond a threshold value $\Omega \geq 0.56$, the system does not show any complex frequency in the k_y direction, indicating the stable behavior. Only the presence of real frequency in the k_y direction indicates a metastable state; also the axial symmetry is preserved [see Figs. 4(d1) and 4(d2)]. Overall, we find that the increase in the Rabi coupling strength for a fixed k_L leads to the stabilization of the system. From the excitation spectrum, we analyzed the phonon-maxon-roton modes. Now, in order to get more insight about the stability of these modes, we move to the analysis of the characteristics of the eigenvectors in the momentum space. Figure 5 shows the eigenvectors corresponding to the eigenspectrum given in the Fig. 4. The first row displays the eigenvectors corresponding to $\omega_+(k_x, 0)$, while the second and third rows demonstrate the eigenvectors of $\omega_-(k_x, 0)$ and $\omega_-(0, k_y)$, respectively. For $\Omega = 0$ with $k_L = 0.75$, both eigenvectors in the k_x momentum direction are in-phase, except near $k_x = 0$. At $k_x = 0$, both u and v become equal, indicating the presence of a phonon mode and absence of a maxon mode. However, for ω_- , we observe a complicated spin-flipping behavior in both the k_x and k_y directions of the eigenvectors, which is with respect to the negative and imaginary eigenfrequency of the excitation spectrum.

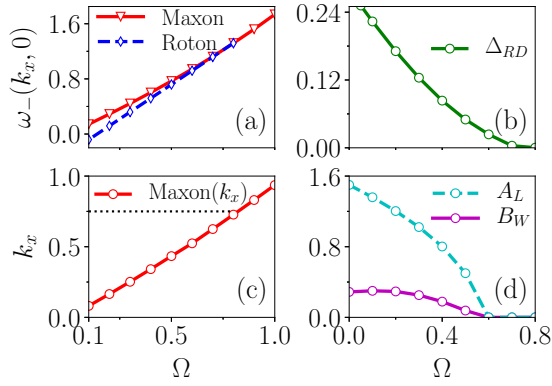


FIG. 6. Variation of different quantities with Ω for $\alpha = 1$, $\beta = 1$ and $k_L = 0.75$. (a) Variation of maxon (red open inverted triangles) and roton minima (blue open diamond). (b) Decay in roton depth (Δ_{RD}). (c) Position of maxon (red open circles) and roton minima (black dotted lines) in the k_x momentum direction. (d) Amplitude loss in instability (cyan open circles) and the corresponding bandwidth (magenta circles) in the k_y momentum space.

Similar to the earlier studies [57,66,68,69], we observe the two branches in the spectrum. The first one represents the gapless density mode (in-phase mode) corresponding to the Goldstone mode with U(1) symmetry and the second one denotes the gapped spin mode (out-of-phase mode). As we carefully analyze their corresponding eigenmodes, we notice some important differences. On one hand, for the density mode, we obtain $|u_\uparrow|^2 - |u_\downarrow|^2 = |v_\uparrow|^2 - |v_\downarrow|^2 = 0$, which in terms of spin language is an unpolarized mode, while on the other hand, for the spin mode, we find breaking of the \mathbb{Z}_2 symmetry, meaning that $|u_\uparrow|^2 - |u_\downarrow|^2 \neq 0$ and $|v_\uparrow|^2 - |v_\downarrow|^2 \neq 0$ that implies a polarized mode in the spin language [69].

Overall, we find for $\Omega < 0.6$ [Figs. 4(a1)–4(c1)], when the excitation spectra exhibit complex eigenvalues indicating the dynamical instability, the corresponding eigenvectors (Fig. 5) of such excitation spectra show the presence of spin modes. An increase in the value of Ω to $\Omega = 0.6$ results in the complete suppression of such unstable spin mode and the emergence of the density mode in the system. The same scenario appears to be present for the parameters of Fig. 7, where an increase of k_L generates dynamical instabilities in the system that manifest as the emergence of the spin modes.

We also analytically compute the effect of Ω with fixed parameters $k_L = 0.75$, $\alpha = \beta = 1$ on the maxon and roton minimum from the collective excitation spectrum. In Fig. 6(a), using a solid red line with triangle, we show the maxon, and using a blue line with diamond, we represent the roton minimum. The points corresponding to the maxons and rotors are well fitted with the straight line beyond the critical value of Ω , where both the points corresponding to the maxon-roton appear to merge, as clearly depicted in Fig. 6(a). The difference between the roton minimum and maxon gives the roton depth (Δ_{RD}), as displayed in Fig. 6(b). As the Rabi coupling is increased, the minima corresponding to the roton disappears. Beyond the critical value, only the maxon in the k_x direction is observed (see Fig. 4). We find that the outcome of increase in the Rabi coupling strength is the decay of the roton depth.

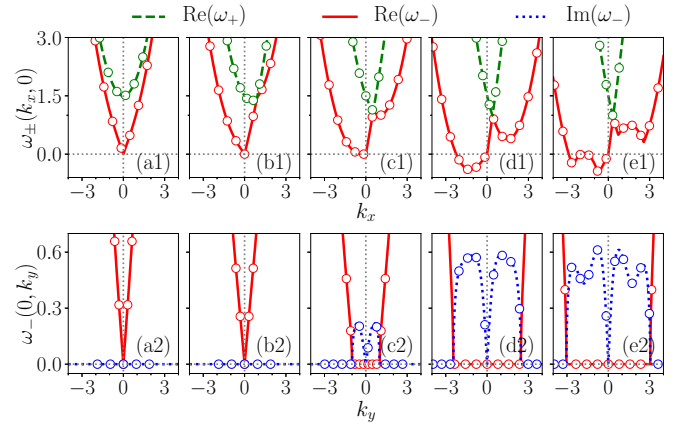


FIG. 7. Variation of excitation spectrum in the k_x (first row) and k_y (second row) momentum directions for different SO coupling strengths k_L , which varies in (a)–(e) = (0, 0.5, 1.0, 1.5, 1.75). Other parameters are $\Omega = 0.75$, $\alpha = \beta = 1$. First row: Green dashed and solid red lines indicate $\omega_+(k_x, 0)$ and $\omega_-(k_x, 0)$, respectively. Second row: solid red and blue dotted lines show $\text{Re}[\omega_-(0, k_y)]$ and $|\text{Im}[\omega_-(0, k_y)]|$, respectively. Solid lines are analytical results from Eq. (15) and open circles are numerically obtained from Eq. (12). The increase in k_L leads to the generation of imaginary energy frequency modes in the k_y direction.

These observations are consistent with previous theoretical models [37,38,49] and experiments [39–42].

In Fig. 6(c), we show the change in the positions of the maxon and roton minimum positions along the k_x momentum space with the Rabi coupling (Ω). We find that the roton minima are always present at $k_x = 0.75$, which appears to be similar to what we observed for the fixed Rashba SO coupling strength $k_L = 0.75$. However, upon looking at the behavior carefully, we find that the position of the maxon increases upon increase of the Rabi coupling strength and, finally, at $\Omega \approx 0.8$, the maxon and the roton merge. As a consequence of this, for $\Omega > 0.8$, only the maxon appears to be present in the system. In a similar way, we notice the loss in the amplitude of the instability (denoted as A_L) upon increase of Ω . In Fig. 6(d), we plot the variation of A_L and instability bandwidth (B_W) with the Rabi coupling, which clearly complement our results attributed to the stabilization of the system beyond $\Omega \approx 0.8$.

D. Role of Rashba spin-orbit coupling (k_L)

In this section, we investigate the effect of Rashba couplings on the excitation spectrum by fixing the other parameters, such as $\Omega = 0.75$ and $\alpha = \beta = 1$. In the absence of Rashba coupling ($k_L = 0$), we find that the spectrum only has the real frequencies which are symmetric in both the k_x and k_y directions. We also explore the zero momentum phase [see Figs. 7(a1) and 7(a2)]. As the Rashba coupling is raised to $k_L = 0.1$, the maxon mode appears in the system. Further increase in k_L ($=0.5$) leads to the generation of a roton minimum in the spectrum, as shown in Fig. 7(b1). For $k_L > 0.86$, we find a transition from the stable to the unstable state, which is quite evident by the presence of complex frequencies in the k_y directions of the $\omega_-(0, k_y)$ spectrum, as shown in Fig. 7(c2). Further increase in k_L results in enhancement in the magnitude

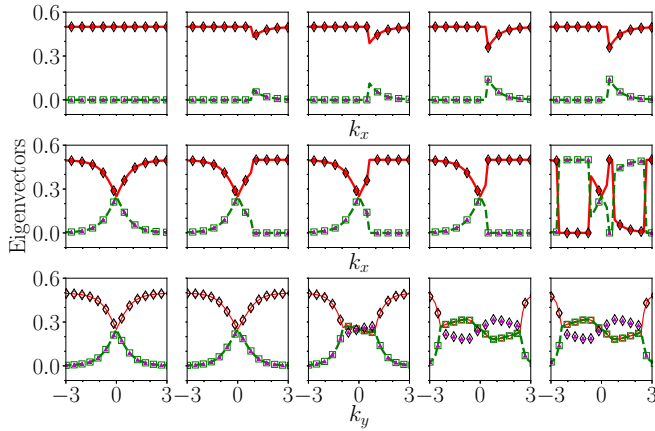


FIG. 8. Eigenvectors associated with Fig. 7, which are obtained numerically from Eq. (15). The representation of the eigenvector components is the same as in Fig. 3. First row: $\omega_+(k_x, 0)$; second row: $\omega_-(k_x, 0)$; third row: $\omega_-(0, k_y)$. The first row shows the evolution of the maxon modes, the second row displays phonon-maxon to complicated spin-flipping modes, and the third row clearly shows the transition from density to spin mode.

of the instability [see Fig. 7(d2)]. For $k_L > 1.5$, we notice the negative frequency with two minima in the k_x direction, which gives two stability bands in both sides of the k_y direction [see Figs. 7(e1) and 7(e2)]. We find that the role of SO coupling here is to gradually increase the phonon-maxon and roton minimum up to the critical value of k_L in k_x momentum space. Increasing k_L beyond a critical value leads to the loss of the phonon-maxon and roton minimum as part of having the negative energy that shows the system becomes energetically unstable and thus lacks any superfluidity [49].

In Fig. 8, we plot the eigenvectors corresponding to the eigenspectrum, as shown in Fig. 7. For the $k_L \neq 0$ cases, in the $\omega_+(k_x, 0)$ spectrums, the u (v) exhibit a decreasing (increasing) trend to reach the point of the maxon mode, which also shows the coupling point between the local minimum of $\omega_+(k_x, 0)$ and the maxon of $\omega_-(k_x, 0)$. In the k_y momentum direction, we initially notice the presence of density modes that get transmuted to spin-density modes as k_L is increased for fixed Ω (Fig. 8, third row). Through the eigenvector analysis, we establish the existence of phonon-maxon modes.

E. Stability phase diagram

In order to provide a detailed picture of the stability of the ground-state phases, we identify a phase transition from a stable to unstable phase in the $k_L - \Omega$ plane using an excitation spectrum, and illustrate this in the phase diagram shown in Fig. 9. By simultaneously varying Ω and k_L , we note the critical point at fixed $k_x = 0$, where the transition from the real to the complex frequencies takes place. These critical points are shown with the green dots in the $k_L - \Omega$ plane. We characterize the phase as a stable one if the frequencies are real, otherwise the phase is denoted as unstable for the complex frequencies [45,49,66].

One may note that the BdG analysis presented in the previous section considers homogeneous BECs, whereas the experimental system, in general, is confined under the

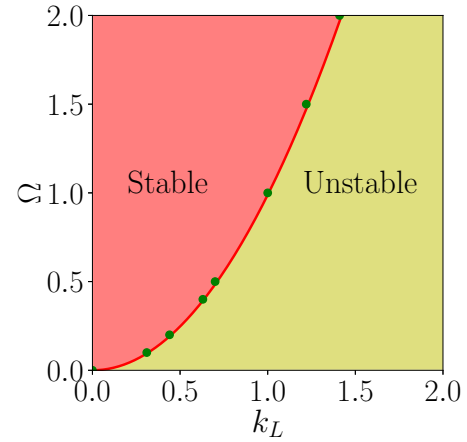


FIG. 9. Stability phase diagram illustrating the stable and unstable phases in the $k_L - \Omega$ plane with fixed weak repulsive nonlinear contact interaction strengths, $\alpha = \beta = 1$. Green dots represent the phase transition points of the unstable and stable boundary obtained from the eigenspectrum using Eq. (15).

harmonic trap [9]. This inconsistency in the model can be managed if the density of homogeneous BECs is taken to be equal to the central density of the trapped BECs while obtaining the ground-state phases. For further details, readers may refer to Refs. [40–42]. Experimentally, the collective excitation spectrum can be realized using the Bragg spectroscopy technique, wherein Bragg laser beams are applied on the condensates in about a few milliseconds, which further supplies a momentum kick corresponding to the perturbation ($\delta\psi$) to the ground-state wave function (ψ) and produces excitations. In experiment, the momentum transfer can be calculated by the frequency difference between the Bragg laser beams [42]. Changing the Bragg laser wavelength and geometry provides an interesting rotonlike structure. Once the roton appears, the atoms can be transferred to the roton minimum, and a large variety of collective excitation modes can be obtained by tuning the Rabi and SO coupling strengths [40–42].

Having attained a fair understanding of the different phases of the excitation spectrum of the coupled BECs using BdG equations, in the following section we complement our observation by directly solving the set of SO coupled binary GP equations.

V. DYNAMICAL STABILITY ANALYSIS USING NUMERICAL SIMULATION

In this section, we present the numerical results which are obtained by solving the dynamical equations [Eqs. (4)] of the coupled BECs. We use the imaginary-time propagation (ITP) method to obtain the ground state of the system. Subsequently, we evolve the ground-state wave function by using the conventional real-time propagation (RTP), where, in both methods, we adopted the split-step Crank-Nicholson scheme [70–73]. We have considered the grid sizes 400×400 with space steps $dx = dy = 0.1$, and time step $dt = 0.005$ is used. Initially, we obtained the ground-state wave functions using the ITP method with respect to a stable ($k_L = 0, \Omega = 0.75$) and unstable ($k_L = 1.5, \Omega = 0.75$) regime of the stability

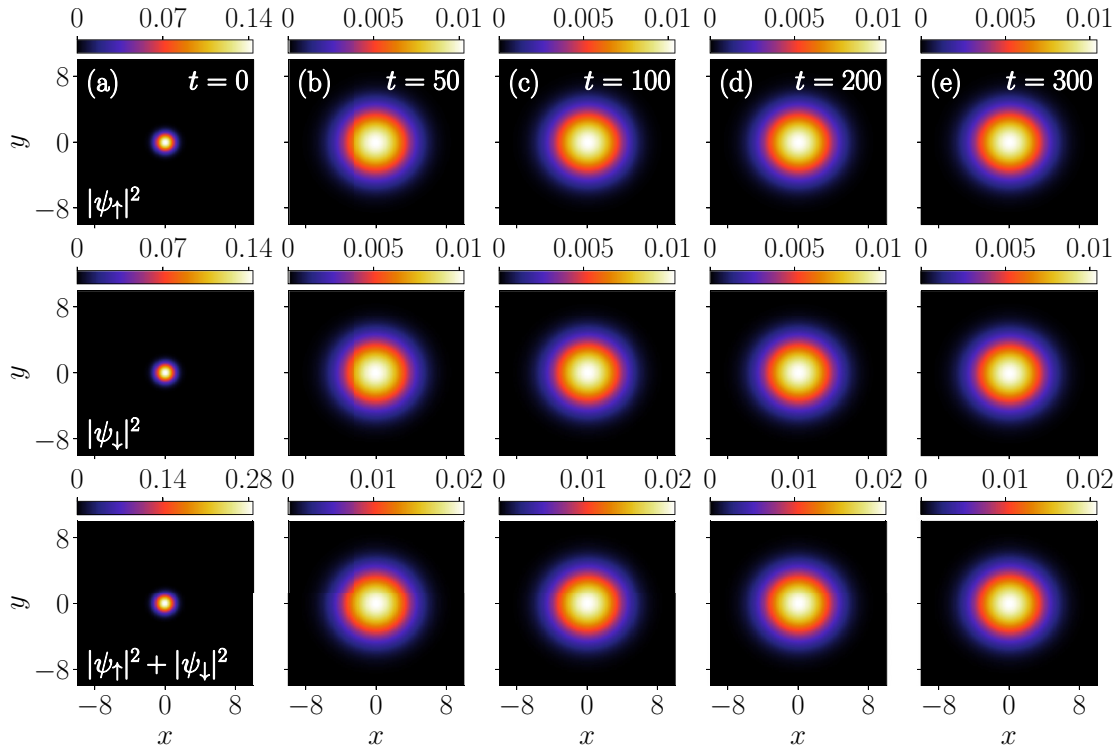


FIG. 10. Time evolution of the ground-state density for $\Omega = 0.75$, $k_L = 0$, and $\alpha = \beta = 1$. (a) The first column shows the actual ground-state wave functions obtained from the imaginary-time propagation method at $t = 0$. (b)–(e) Their dynamical density patterns at different time instants $t = 50, 100, 200, 300$, respectively. Top row: spin-up ($|\psi_\uparrow|^2$) density; middle row: spin-down ($|\psi_\downarrow|^2$) density; and bottom row: total density ($|\psi_\uparrow|^2 + |\psi_\downarrow|^2$).

phase diagram of Fig. 9. Once the ground-state wave function is obtained, we then evolve it by employing the RTP method, in which we quench the system by reducing the trap strength as $\lambda = \kappa = 1.0 \rightarrow 0.5$ at $t = 0$.

To begin with, we consider the parameters $\Omega = 0.75$, $k_L = 0$ and $\alpha = \beta = 1$ with $\lambda = \kappa = 1$ that lie in the stable region. For these parameters, we find that the ground-state wave function is of a plane-wave (PW) nature [see Fig. 10(a)]. In order to analyze the stability of this state, we evolved the ground-state wave function using RTP. In Figs. 10(b)–10(h), we show the temporal evolution of the ground state up to $t = 300$. As we look at the evolution carefully, we find that as time progresses, the condensate experiences the expansion due to the presence of repulsive interactions. So to stabilize against the expansion, a trap is added [28]. At $t = 0$, owing to sudden lowering of the trap strength by half, the condensate expands for a time interval $0 < t < 50$ [see Fig. 7(b)]. For $t > 50$, the size of the condensate does not change and the system attains the stable steady state [Figs. 10(c)–10(e)]. This is evident from the evolution of the density of each spin component as shown in the top and middle rows of Figs. 10. Also, a similar feature can be seen for the total density (bottom row of Figs. 10). Moreover, we find that the density profiles of both of the components are symmetric in nature and do not exhibit any oscillations (Fig. 11). Thus they lack any polarization, which is also quite evident from the behavior of the eigenvectors that clearly shows the presence of the Goldstone mode (in-phase mode) [57,69] (see first column of Fig. 8).

In order to verify the dynamics of the condensate, next we calculate the root-mean-square (rms) size of the condensate. Initially, we find that the condensate diffuses after the trap is quenched. The rms sizes of $\langle x^2 \rangle$, $\langle y^2 \rangle$, and $\langle r^2 \rangle$ are illustrated in Fig. 12(a). The peak densities of both components $\max(|\psi_{\uparrow,\downarrow}|^2)$ and $\max(|\psi_\uparrow|^2 + |\psi_\downarrow|^2)$ decrease for a while; thereafter, they attain a steady state, which is shown in Fig. 12(b). However, the condensate size in both the x and y directions is the same, as well as the maximum density of both components which have a similar feature. In Fig. 12(c), we plot the temporal evolution of the energy, which confirms

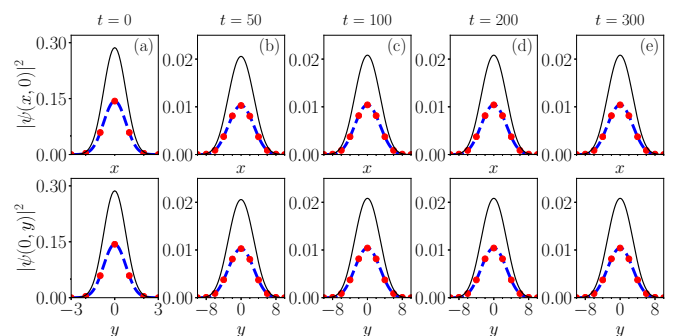


FIG. 11. One-dimensional density patterns corresponding to Fig. 10. The first row represents the x -direction densities where $y = 0$, and the second row represents the y -direction densities for $x = 0$; $|\psi_\uparrow|^2$ (red dots), $|\psi_\downarrow|^2$ (blue dashed line), $|\psi_\uparrow|^2 + |\psi_\downarrow|^2$ (black solid line).

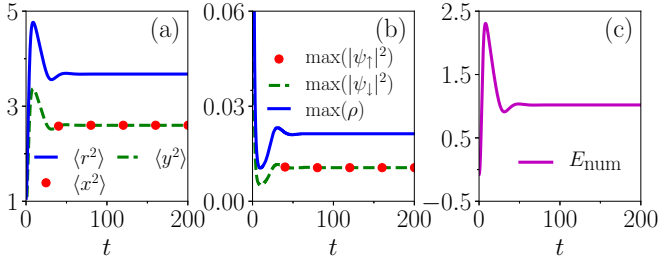


FIG. 12. (a) Time evolution of root-mean-square (rms) size in $\langle x^2 \rangle$ (solid red dots), $\langle y^2 \rangle$ (dashed green line), and $\langle r^2 \rangle$ (solid blue line) directions. (b) The maximum of density $\max(|\psi_{\uparrow,\downarrow}|^2)$ (solid red dots and dashed green lines), $\max(|\psi_{\uparrow}|^2 + |\psi_{\downarrow}|^2)$ (solid blue line) and (c) total system energy. The parameters are the same as in Fig. 10.

that the system attains the steady state after $t > 50$, which is consistent with the evolution of the density profile. As we analyze the condensate evolution more carefully, as shown in Figs. 10 and 12, we find that the ground state is dynamically and energetically stable. It also coincides with the stability regime in the phase diagram of Fig. 9, which we get from the BdG excitation spectrum.

In order to gain more insight into the behavior of the condensate, we also analyze the dynamics of the instability regime, which is investigated by fixing the parameters as $\Omega = 0.75$, $k_L = 1.5$, and $\alpha = \beta = 1$ with trap strength $\lambda = \kappa = 1$. We obtain the ground state as an elongated plane-wave phase, as illustrated in Fig. 13(a). However, the BdG excitation spectrum has a negative energy minimum as well as complex

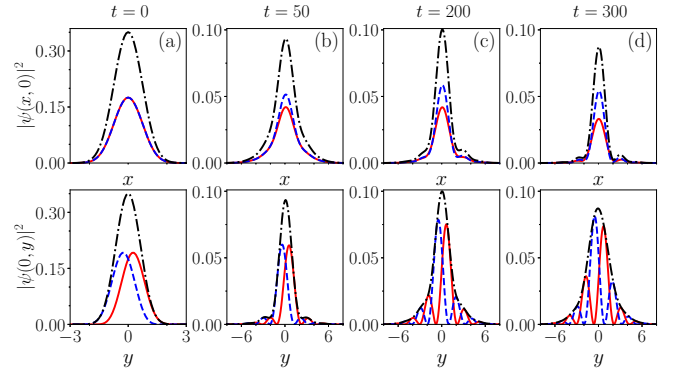


FIG. 14. One-dimensional density patterns as in Fig. 11. The parameters correspond to Fig. 13; $|\psi_{\uparrow}|^2$ (solid red line), $|\psi_{\downarrow}|^2$ (blue dashed line), $|\psi_{\uparrow}|^2 + |\psi_{\downarrow}|^2$ (black dash-dotted line).

eigenfrequencies [see Fig. 7(d)] in the k_x and k_y directions, respectively. This feature indicates that the system is energetically [see Fig. 15(c)] and dynamically [see Figs. 13(b)–13(e)] unstable. Apart from this, we also capture the temporal evolution of the density corresponding to each spin component along with the total density, as shown in Fig. 14. Note that these wave functions are also related to the spinlike mode [57,69], as is quite evident from the nature of the eigenvectors in Fig. 8 (fourth column). In Fig. 15, we show the dynamical evolution of different physical quantities, such as the root-mean-square size of the condensate, maximum of the density, and total energy of the system. As we look at the evolution of the condensate rms size in the x and y directions, as illustrated

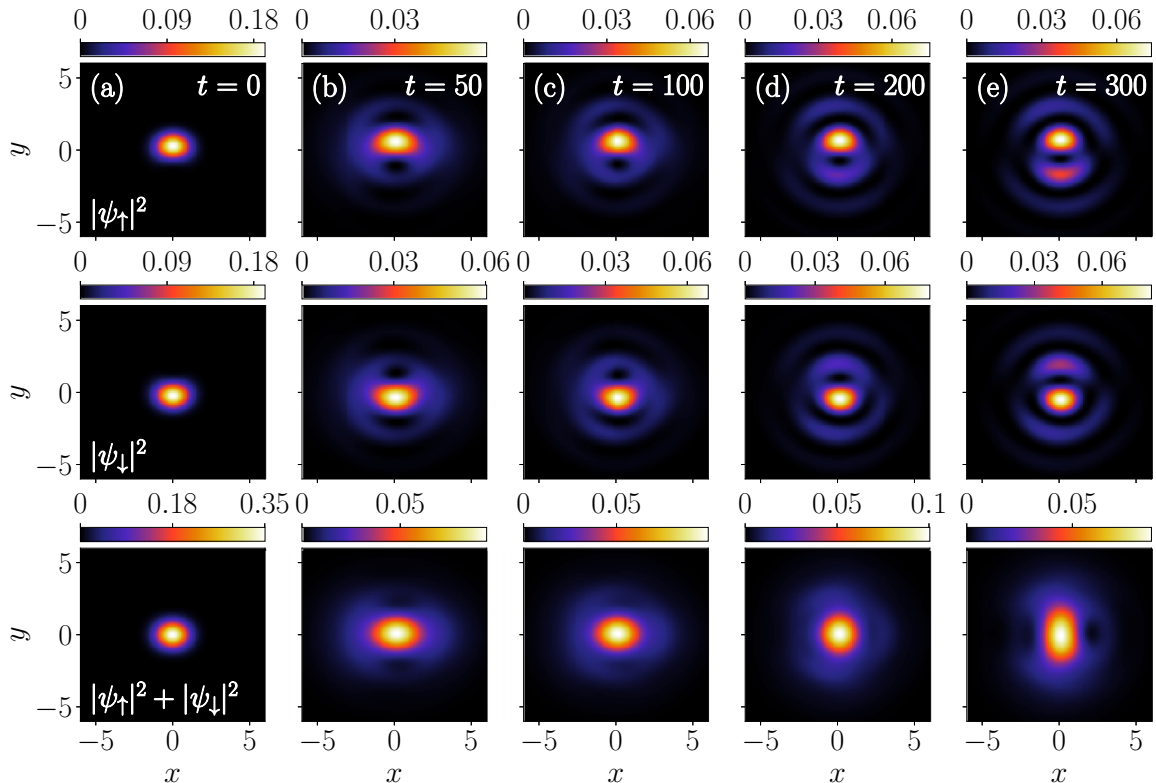


FIG. 13. Dynamics of ground-state density in the x - y plane, same as in the Fig. 10, for parameters $k_L = 1.5$, $\Omega = 0.75$, with $\alpha = \beta = 1$.

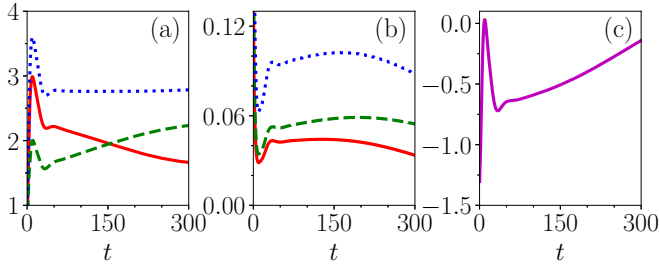


FIG. 15. (a) Time evolution of the root-mean-square (rms) size in the $\langle x^2 \rangle$ (solid red line), $\langle y^2 \rangle$ (dashed green line), and $\langle r^2 \rangle$ (dotted blue line) directions. (b) The maximum of density $\max(|\psi_{\uparrow,\downarrow}|^2)$ (solid red and dashed green lines), $\max(|\psi_{\uparrow}|^2 + |\psi_{\downarrow}|^2)$ (dotted blue line), and (c) total system energy. The parameters are the same as in Fig. 13.

in Fig. 15(a), we find the condensate size decreases in the x direction while it increases in the y direction with time. However, the spin components are polarized, which leads to the emergence of an interference pattern as time progresses. This suggests the presence of instability in the system, which manifestation can also be seen in the temporal evolution of the total density profile as shown in the bottom row of Fig. 13. Here the density profile that initially was quite symmetric in both directions becomes elongated along the y direction at $t = 300$. The other way in which we can characterize the unstable nature of the condensate is by looking at the temporal evolution of the maximum of the density corresponding to the spin component. Figure 15(b) depicts the evolution of the maximum of the spin component as well as the maximum corresponding to the total density. After $t \gtrsim 150$, we notice a gradual decrease in their values, signifying the unstable behavior. Finally, we show the temporal evolution of the total condensate energy in Fig. 15(c). We find a sharp increase in the total energy beyond $t \gtrsim 20$, which clearly indicates the dynamically unstable nature of the condensate.

VI. SUMMARY AND CONCLUSIONS

In this paper, we have investigated the collective excitation spectrum of Rashba SO coupled Bose-Einstein condensates, with Rabi mixing in two dimensions using the Bogoliubov-de Gennes theory. First we have analyzed the dispersion of a single-particle system in the momentum space, in which, as a consequence of Rabi coupling, the system has broken rotational symmetry, as k_x momentum space has lower ground-state energy compared with the k_y momentum direction. Following this, we have presented the excitation spectrum with and without nonlinear contact interactions. In the case of a noninteracting system, excitations have real negative frequencies, implying that the system is energetically unstable. For the interacting case, increases in the Rabi strength (Ω) for fixed k_L lead the system to make a transition from the unstable phase to the stable phase. We find that the phonon-maxon-roton modes disappear upon increase of the

Rabi strengths that leads to the loss of the roton depth. The position of the roton minimum is only present at $k_x = k_L$, and the maxon position is approximately equal to the Rabi strengths. The increase of Rabi coupling strength results in the loss of instability and bandwidth. However, in contrast to the Rabi coupling, the SO Rashba coupling has a destabilizing effect. Further, the Rashba SO coupling turns a symmetric system into an asymmetric one. By increasing the k_L , the phonon-maxon-roton modes and instability are revealed in the k_x and k_y momentum directions. After a critical value of k_L , we have negative frequency, and additional increase in k_L shows a double minimum in the k_x and two instability bands in the k_y momentum directions. Due to negative and complex frequencies, the system lacks superfluidity and supersolidity, even though it exhibits double roton minima.

We confirm the observation of the BdG spectrum by directly solving the coupled GP equations. We find the presence of a plane wave and elongated plane wave in the parameter ranges where the BdG spectrum exhibits the stable and unstable phases, respectively. Their size and maximum of density and energies are studied in the time evolution, which clearly explains the dynamic and energetic stability and instability phases, that also confirms the phenomena obtained from the excitation spectrum.

In further studies, it would be interesting to extend the studies present here for the denser regime, where three-body interactions become relevant. As predicted in Ref. [54], it may lead to the stabilization of the system and occurrence of different supersolid phases. In another direction, it would also be interesting to analyze the interplay between the SO couplings and quantum fluctuations, which appears to stabilize the condensates and leads to the formation of droplets [52], on the overall stability of the BdG spectrum in a similar line as the present study.

ACKNOWLEDGMENTS

R.R. acknowledges DST-SERB (Department of Science and Technology - Science and Engineering Research Board) for the financial support through Project No. ECR/2017/002639 and UGC (University Grants Commission) for financial support in the form of a UGC-BSR-RFSMS Research Fellowship scheme (2015-2020). A.G. acknowledges FAPESP 2016/17612-7 and CNPq (Conselho Nacional de Desenvolvimento Científico e Tecnológico) Grant No. 306920/2018-2. The work of P.M. is supported by CSIR (Council of Scientific and Industrial Research) under Grant No. 03(1422)/18/EMR-II, DST-SERB under Grant No. CRG/2019/004059, FIST (Department of Physics), DST-PURSE and MHRD RUSA 2.0 (Physical Sciences) Programmes, and FAPESP (Fundação de Amparo à pesquisa do Estado de São Paulo) Grant No. 2016/00269-8. P.K.M. acknowledges DST-SERB for the financial support through Project No. ECR/2017/002639.

APPENDIX A: A CALCULATION OF ENERGY OF SO COUPLED BECS

In this Appendix, we provide the detailed steps to obtain the total energy of the SO coupled BECs. We substitute the stationary state form of the wave function given in Eq. (6) into Eq. (4), and further separate the real and imaginary parts,

which yields

$$\mu_{\uparrow}\psi_{\uparrow R} = \left[-\frac{1}{2}\frac{\partial^2}{\partial x^2} - \frac{1}{2}\frac{\partial^2}{\partial y^2} + V_{2D}(x, y) + \alpha|\psi_{\uparrow}|^2 + \beta|\psi_{\downarrow}|^2 \right] \psi_{\uparrow R} + k_L \left(\frac{\partial\psi_{\downarrow I}}{\partial x} - \frac{\partial\psi_{\downarrow R}}{\partial y} \right) + \Omega\psi_{\downarrow R}, \quad (\text{A1a})$$

$$\mu_{\downarrow}\psi_{\downarrow R} = \left[-\frac{1}{2}\frac{\partial^2}{\partial x^2} - \frac{1}{2}\frac{\partial^2}{\partial y^2} + V_{2D}(x, y) + \beta|\psi_{\uparrow}|^2 + \alpha|\psi_{\downarrow}|^2 \right] \psi_{\downarrow R} + k_L \left(\frac{\partial\psi_{\uparrow I}}{\partial x} + \frac{\partial\psi_{\uparrow R}}{\partial y} \right) + \Omega\psi_{\uparrow R}, \quad (\text{A1b})$$

and for the imaginary parts, we have

$$\mu_{\uparrow}\psi_{\uparrow I} = \left[-\frac{1}{2}\frac{\partial^2}{\partial x^2} - \frac{1}{2}\frac{\partial^2}{\partial y^2} + V_{2D}(x, y) + \alpha|\psi_{\uparrow}|^2 + \beta|\psi_{\downarrow}|^2 \right] \psi_{\uparrow I} - k_L \left(\frac{\partial\psi_{\downarrow R}}{\partial x} + \frac{\partial\psi_{\downarrow I}}{\partial y} \right) + \Omega\psi_{\downarrow I}, \quad (\text{A1c})$$

$$\mu_{\downarrow}\psi_{\downarrow I} = \left[-\frac{1}{2}\frac{\partial^2}{\partial x^2} - \frac{1}{2}\frac{\partial^2}{\partial y^2} + V_{2D}(x, y) + \beta|\psi_{\uparrow}|^2 + \alpha|\psi_{\downarrow}|^2 \right] \psi_{\downarrow I} - k_L \left(\frac{\partial\psi_{\uparrow R}}{\partial x} - \frac{\partial\psi_{\uparrow I}}{\partial y} \right) + \Omega\psi_{\uparrow I}, \quad (\text{A1d})$$

where $|\psi_{\uparrow}|^2 = \psi_{\uparrow R}^2 + \psi_{\uparrow I}^2$ and $|\psi_{\downarrow}|^2 = \psi_{\downarrow R}^2 + \psi_{\downarrow I}^2$. Multiplying Eq. (A1a) with $\psi_{\uparrow R}$ and Eq. (A1b) with $\psi_{\downarrow R}$, and integrating, we get

$$\mu_{\uparrow} \int dx dy \psi_{\uparrow R}^2 = \int dx dy \psi_{\uparrow R} \left\{ \left[-\frac{1}{2}\frac{\partial^2}{\partial x^2} - \frac{1}{2}\frac{\partial^2}{\partial y^2} + V_{2D}(x, y) + \alpha|\psi_{\uparrow}|^2 + \beta|\psi_{\downarrow}|^2 \right] \psi_{\uparrow R} + k_L \left(\frac{\partial\psi_{\downarrow I}}{\partial x} - \frac{\partial\psi_{\downarrow R}}{\partial y} \right) + \Omega\psi_{\downarrow R} \right\}, \quad (\text{A2a})$$

$$\mu_{\downarrow} \int dx dy \psi_{\downarrow R}^2 = \int dx dy \psi_{\downarrow R} \left\{ \left[-\frac{1}{2}\frac{\partial^2}{\partial x^2} - \frac{1}{2}\frac{\partial^2}{\partial y^2} + V_{2D}(x, y) + \beta|\psi_{\uparrow}|^2 + \alpha|\psi_{\downarrow}|^2 \right] \psi_{\downarrow R} - k_L \left(\frac{\partial\psi_{\uparrow I}}{\partial x} + \frac{\partial\psi_{\uparrow R}}{\partial y} \right) + \Omega\psi_{\uparrow R} \right\}. \quad (\text{A2b})$$

Rearranging the above equations yields

$$\begin{aligned} \mu_{\uparrow} &= \frac{1}{\int \psi_{\uparrow R}^2 dx dy} \int \left\{ \frac{1}{2} \left(\frac{\partial\psi_{\uparrow R}}{\partial x} \right)^2 + \frac{1}{2} \left(\frac{\partial\psi_{\uparrow R}}{\partial y} \right)^2 + [V_{2D}(x, y) + \alpha|\psi_{\uparrow}|^2 + \beta|\psi_{\downarrow}|^2] \psi_{\uparrow R}^2 \right\} dx dy \\ &\quad + \frac{1}{\int \psi_{\uparrow R}^2 dx dy} \int \left[k_L \left(\frac{\partial\psi_{\downarrow I}}{\partial x} - \frac{\partial\psi_{\downarrow R}}{\partial y} \right) + \Omega\psi_{\downarrow R} \right] \psi_{\uparrow R} dx dy, \end{aligned} \quad (\text{A3a})$$

$$\begin{aligned} \mu_{\downarrow} &= \frac{1}{\int \psi_{\downarrow R}^2 dx dy} \int \left\{ \frac{1}{2} \left(\frac{\partial\psi_{\downarrow R}}{\partial x} \right)^2 + \frac{1}{2} \left(\frac{\partial\psi_{\downarrow R}}{\partial y} \right)^2 + [V_{2D}(x, y) + \beta|\psi_{\uparrow}|^2 + \alpha|\psi_{\downarrow}|^2] \psi_{\downarrow R}^2 \right\} dx dy \\ &\quad + \frac{1}{\int \psi_{\downarrow R}^2 dx dy} \int \left[k_L \left(\frac{\partial\psi_{\uparrow I}}{\partial x} + \frac{\partial\psi_{\uparrow R}}{\partial y} \right) + \Omega\psi_{\uparrow R} \right] \psi_{\downarrow R} dx dy. \end{aligned} \quad (\text{A3b})$$

From this, we get the total energy given by $E_{\text{num}} = \sum_{j=\uparrow, \downarrow} \frac{\int \int (E_j^{2C} + E_j^{\text{SO}}) dx dy}{\int \int \psi_j^2 dx dy}$, which can be extracted from the above chemical potential equations as

$$E_{\uparrow}^{2C} = (\partial_x^2 \psi_{\uparrow R})^2 + (\partial_y^2 \psi_{\uparrow R})^2 + (V_{2D} + \alpha|\psi_{\uparrow}|^2/2 + \beta|\psi_{\downarrow}|^2/2) \psi_{\uparrow R}^2, \quad (\text{A4a})$$

$$E_{\downarrow}^{2C} = (\partial_x^2 \psi_{\downarrow R})^2 + (\partial_y^2 \psi_{\downarrow R})^2 + (V_{2D} + \beta|\psi_{\uparrow}|^2/2 + \alpha|\psi_{\downarrow}|^2/2) \psi_{\downarrow R}^2, \quad (\text{A4b})$$

$$E_{\uparrow}^{\text{SO}} = k_L (\psi_{\uparrow R} \partial_x \psi_{\downarrow I} - \psi_{\uparrow R} \partial_y \psi_{\downarrow R}) + \psi_{\uparrow R} \Omega \psi_{\downarrow R}, \quad (\text{A4c})$$

$$E_{\downarrow}^{\text{SO}} = k_L (\psi_{\downarrow R} \partial_x \psi_{\uparrow I} + \psi_{\downarrow R} \partial_y \psi_{\uparrow R}) + \psi_{\downarrow R} \Omega \psi_{\uparrow R}. \quad (\text{A4d})$$

APPENDIX B: ELEMENTS OF THE BDG MATRIX

$$f(n_{\uparrow}, n_{\downarrow}) = \frac{(k_x^2 + k_y^2)}{2} + 2\alpha n_{\uparrow} + \beta n_{\downarrow} - \mu, \quad (\text{B1a})$$

$$g(n_{\uparrow}, n_{\downarrow}) = \frac{(k_x^2 + k_y^2)}{2} + \alpha n_{\uparrow} + 2\beta n_{\downarrow} - \mu, \quad (\text{B1b})$$

$$L_{13(24)} = \beta \sqrt{n_{\uparrow} n_{\downarrow}} \pm k_L (k_x - ik_y) - \Omega, \quad (\text{B1c})$$

$$L_{31(42)} = \beta \sqrt{n_{\uparrow} n_{\downarrow}} \pm k_L (k_x + ik_y) - \Omega, \quad (\text{B1d})$$

where

$$\mu = \frac{1}{2} \left[\alpha(n_{\uparrow} + n_{\downarrow}) + \beta n - \frac{n\Omega}{\sqrt{n_{\uparrow}n_{\downarrow}}} \right].$$

APPENDIX C: COEFFICIENTS OF THE BDG EXCITATION SPECTRUM

$$b = -(k_x^2 + k_y^2) \left[2(k_L^2 + \Omega)\alpha + \frac{1}{2}(k_x^2 + k_y^2) \right] - 2\Omega[(\alpha - \beta) + 2\Omega], \quad (\text{C1a})$$

$$c = 2k_L k_x \{ 2\Omega[(\alpha - \beta) + 2\Omega] - (k_x^2 + k_y^2)(\beta - 2\Omega) \}, \quad (\text{C1b})$$

$$d = \frac{1}{16} \{ (k_x^8 + k_y^8) + 4P(k_x^6 + k_y^6) + 2Q(k_x^4 + k_y^4) + k_x^2 k_y^2 [(k_x^4 + k_y^4) + 12P(k_x^2 + k_y^2) + 6k_x^2 k_y^2 + 4Q] \} + (Rk_x^2 + Sk_y^2), \quad (\text{C1c})$$

where

$$P = \alpha - 2k_L^2 + 2\Omega, \quad (\text{C2a})$$

$$Q = 2[\alpha^2 - \beta^2 + \alpha(6\Omega - 4k_L^2) + 2\beta\Omega + 4(k_L^2 - \Omega)^2], \quad (\text{C2b})$$

$$R = \Omega(\alpha + \beta - 2k_L^2)(\alpha - \beta + 2\Omega), \quad (\text{C2c})$$

$$S = \Omega(\alpha + \beta)(\alpha - \beta - 2k_L^2 + 2\Omega). \quad (\text{C2d})$$

-
- [1] M. H. Anderson, J. R. Ensher, M. R. Matthews, C. E. Wieman, and E. A. Cornell, *Science* **269**, 198 (1995).
- [2] K. B. Davis, M. O. Mewes, M. R. Andrews, N. J. van Druten, D. S. Durfee, D. M. Kurn, and W. Ketterle, *Phys. Rev. Lett.* **75**, 3969 (1995).
- [3] C. C. Bradley, C. A. Sackett, J. J. Tollett, and R. G. Hulet, *Phys. Rev. Lett.* **75**, 1687 (1995).
- [4] J. M. Gerton, D. Strekalov, I. Prodan, and R. G. Hulet, *Nature (London)* **408**, 692 (2000).
- [5] M. Greiner, O. Mandel, T. Esslinger, T. W. Hänsch, and I. Bloch, *Nature (London)* **415**, 39 (2002).
- [6] O. Morsch and M. Oberthaler, *Rev. Mod. Phys.* **78**, 179 (2006).
- [7] M. Lewenstein, A. Sanpera, V. Ahufinger, B. Damski, A. Sen(De), and U. Sen, *Adv. Phys.* **56**, 243 (2007).
- [8] G. Roati, C. D'Errico, L. Fallani, M. Fattori, C. Fort, M. Zaccanti, G. Modugno, M. Modugno, and M. Inguscio, *Nature (London)* **453**, 895 (2008).
- [9] C. Chin, R. Grimm, P. Julienne, and E. Tiesinga, *Rev. Mod. Phys.* **82**, 1225 (2010).
- [10] A. Griesmaier, J. Werner, S. Hensler, J. Stuhler, and T. Pfau, *Phys. Rev. Lett.* **94**, 160401 (2005).
- [11] M. Lu, N. Q. Burdick, S. H. Youn, and B. L. Lev, *Phys. Rev. Lett.* **107**, 190401 (2011).
- [12] K. Aikawa, A. Frisch, M. Mark, S. Baier, A. Rietzler, R. Grimm, and F. Ferlaino, *Phys. Rev. Lett.* **108**, 210401 (2012).
- [13] Y.-J. Lin, K. Jiménez-García, and I. B. Spielman, *Nature (London)* **471**, 83 (2011).
- [14] V. Galitski and I. B. Spielman, *Nature (London)* **494**, 49 (2013).
- [15] T.-L. Ho, *Phys. Rev. Lett.* **81**, 742 (1998).
- [16] T. Ohmi and K. Machida, *J. Phys. Soc. Jpn.* **67**, 1822 (1998).
- [17] S. B. Papp, J. M. Pino, and C. E. Wieman, *Phys. Rev. Lett.* **101**, 040402 (2008).
- [18] H. Takeuchi, S. Ishino, and M. Tsubota, *Phys. Rev. Lett.* **105**, 205301 (2010).
- [19] J. Sabbatini, W. H. Zurek, and M. J. Davis, *Phys. Rev. Lett.* **107**, 230402 (2011).
- [20] K. J. H. Law, P. G. Kevrekidis, and L. S. Tuckerman, *Phys. Rev. Lett.* **105**, 160405 (2010).
- [21] L. Wen, Y. Qiao, Y. Xu, and L. Mao, *Phys. Rev. A* **87**, 033604 (2013).
- [22] M. Aidelsburger, M. Atala, M. Lohse, J. T. Barreiro, B. Paredes, and I. Bloch, *Phys. Rev. Lett.* **111**, 185301 (2013).
- [23] N. Goldman, I. Satija, P. Nikolic, A. Bermudez, M. A. Martin-Delgado, M. Lewenstein, and I. B. Spielman, *Phys. Rev. Lett.* **105**, 255302 (2010).
- [24] Z. Wu, L. Zhang, W. Sun, X.-T. Xu, B.-Z. Wang, S.-C. Ji, Y. Deng, S. Chen, X.-J. Liu, and J.-W. Pan, *Science* **354**, 83 (2016).
- [25] B. T. Seaman, M. Krämer, D. Z. Anderson, and M. J. Holland, *Phys. Rev. A* **75**, 023615 (2007).
- [26] S. N. Andrianov and S. A. Moiseev, *Phys. Rev. A* **90**, 042303 (2014).
- [27] P. Vinayagam, R. Radha, S. Bhuvaneswari, R. Ravisankar, and P. Muruganandam, *Commun. Nonlin. Sci. Num. Simul.* **50**, 68 (2017).
- [28] R. Ravisankar, T. Sriraman, L. Salasnich, and P. Muruganandam, *J. Phys. B* **53**, 195301 (2020).
- [29] V. Achilleos, D. J. Frantzeskakis, P. G. Kevrekidis, and D. E. Pelinovsky, *Phys. Rev. Lett.* **110**, 264101 (2013).
- [30] V. Achilleos, J. Stockhofe, P. G. Kevrekidis, D. J. Frantzeskakis, and P. Schmelcher, *Europhys. Lett.* **103**, 20002 (2013).
- [31] J. Jin, S. Zhang, and W. Han, *J. Phys. B* **47**, 115302 (2014).
- [32] B. Li and H. Sakaguchi, *J. Low Temp. Phys.* **175**, 243 (2013).
- [33] Y. Cheng, G. Tang, and S. K. Adhikari, *Phys. Rev. A* **89**, 063602 (2014).
- [34] H. He and Y. Zhang, *Phys. Rev. A* **103**, 053322 (2021).
- [35] S. Pal, A. Roy, and D. Angom, *J. Phys. B* **50**, 195301 (2017).
- [36] S. Pal, A. Roy, and D. Angom, *J. Phys. B* **51**, 085302 (2018).
- [37] G. I. Martone, Y. Li, L. P. Pitaevskii, and S. Stringari, *Phys. Rev. A* **86**, 063621 (2012).
- [38] Y. Li, G. I. Martone, L. P. Pitaevskii, and S. Stringari, *Phys. Rev. Lett.* **110**, 235302 (2013).

- [39] W. Zheng, Z.-Q. Yu, X. Cui, and H. Zhai, *J. Phys. B* **46**, 134007 (2013).
- [40] M. A. Khamehchi, Y. Zhang, C. Hamner, T. Busch, and P. Engels, *Phys. Rev. A* **90**, 063624 (2014).
- [41] L.-C. Ha, L. W. Clark, C. V. Parker, B. M. Anderson, and C. Chin, *Phys. Rev. Lett.* **114**, 055301 (2015).
- [42] S.-C. Ji, L. Zhang, X.-T. Xu, Z. Wu, Y. Deng, S. Chen, and J.-W. Pan, *Phys. Rev. Lett.* **114**, 105301 (2015).
- [43] R. Liao, O. Fialko, J. Brand, and U. Zülicke, *Phys. Rev. A* **92**, 043633 (2015).
- [44] H. Pu and N. P. Bigelow, *Phys. Rev. Lett.* **80**, 1130 (1998).
- [45] T. Ozawa, L. P. Pitaevskii, and S. Stringari, *Phys. Rev. A* **87**, 063610 (2013).
- [46] L. Chen, H. Pu, Z.-Q. Yu, and Y. Zhang, *Phys. Rev. A* **95**, 033616 (2017).
- [47] Z.-F. Yu and J.-K. Xue, *Europhys. Lett.* **121**, 20003 (2018).
- [48] K. T. Geier, G. I. Martone, P. Hauke, and S. Stringari, *Phys. Rev. Lett.* **127**, 115301 (2021).
- [49] Q. Zhu, C. Zhang, and B. Wu, *Europhys. Lett.* **100**, 50003 (2012).
- [50] Z.-Q. Yu, *Phys. Rev. A* **87**, 051606(R) (2013).
- [51] C. R. Cabrera, L. Tanzi, J. Sanz, B. Naylor, P. Thomas, P. Cheiney, and L. Tarruell, *Science* **359**, 301 (2018).
- [52] D. S. Petrov, *Phys. Rev. Lett.* **115**, 155302 (2015).
- [53] S. Sahu and D. Majumder, *J. Phys. B* **53**, 095301 (2020).
- [54] Z.-K. Lu, Y. Li, D. S. Petrov, and G. V. Shlyapnikov, *Phys. Rev. Lett.* **115**, 075303 (2015).
- [55] J.-R. Li, J. Lee, W. Huang, S. Burchesky, B. Shteynas, F. Ç. Top, A. O. Jamison, and W. Ketterle, *Nature (London)* **543**, 91 (2017).
- [56] C. Wang, C. Gao, C.-M. Jian, and H. Zhai, *Phys. Rev. Lett.* **105**, 160403 (2010).
- [57] M. Abad and A. Recati, *Eur. Phys. J. D* **67**, 148 (2013).
- [58] Y. Li, L. P. Pitaevskii, and S. Stringari, *Phys. Rev. Lett.* **108**, 225301 (2012).
- [59] R. Ravisankar, T. Sriraman, and P. Muruganandam, *AIP Conf. Proc.* **2265**, 030022 (2020).
- [60] S. Bhuvaneswari, K. Nithyanandan, and P. Muruganandam, *J. Phys. Commun.* **2**, 025008 (2018).
- [61] N. N. Bogolyubov, *J. Phys. (USSR)* **11**, 23 (1947).
- [62] P. R. Zilsel, *Phys. Rev.* **79**, 309 (1950).
- [63] G. Rickayzen, *Phys. Rev.* **115**, 795 (1959).
- [64] D. S. Jin, J. R. Ensher, M. R. Matthews, C. E. Wieman, and E. A. Cornell, *Phys. Rev. Lett.* **77**, 420 (1996).
- [65] M.-O. Mewes, M. R. Andrews, N. J. van Druten, D. M. Kurn, D. S. Durfee, C. G. Townsend, and W. Ketterle, *Phys. Rev. Lett.* **77**, 988 (1996).
- [66] E. V. Goldstein and P. Meystre, *Phys. Rev. A* **55**, 2935 (1997).
- [67] E. Anderson, Z. Bai, C. Bischof, L. S. Blackford, J. Demmel, J. Dongarra, J. D. Croz, A. Greenbaum, S. Hammarling, A. McKenney, and D. Sorensen, *LAPACK Users' Guide* (SIAM, 1999).
- [68] P. Tommasini, E. J. V. de Passos, A. F. R. de Toledo Piza, M. S. Hussein, and E. Timmermans, *Phys. Rev. A* **67**, 023606 (2003).
- [69] A. Recati and F. Piazza, *Phys. Rev. B* **99**, 064505 (2019).
- [70] P. Muruganandam and S. K. Adhikari, *Comput. Phys. Commun.* **180**, 1888 (2009).
- [71] L. E. Young-S., D. Vudragović, P. Muruganandam, S. K. Adhikari, and A. Balaž, *Comput. Phys. Commun.* **204**, 209 (2016).
- [72] R. Ravisankar, D. Vudragović, P. Muruganandam, A. Balaž, and S. K. Adhikari, *Comput. Phys. Commun.* **259**, 107657 (2021).
- [73] P. Muruganandam, A. Balaž, and S. K. Adhikari, *Comput. Phys. Commun.* **264**, 107926 (2021).